IEEE Access
Multidisciplinary ⋮ Rapid Review ⋮ Open Access Journal

Received 5 November 2023, accepted 19 November 2023, date of publication 27 November 2023,
date of current version 4 December 2023.

Digital Object Identifier 10.1109/ACCESS.2023.3336913

RESEARCH ARTICLE

Simulation-Based Design of the Common-Mode Transformer-Less Hybrid EMI Filter in DC-Fed Motor Drive Systems

SHOTARO TAKAHASHI, (Member, IEEE)
Graduate School of Engineering Science, Akita University, Akita 010-8502, Japan
e-mail: s-takahashi@gipc.akita-u.ac.jp

This work was supported by the Grant-in-Aid for Early-Career Scientists under Grant 23K13315.

ABSTRACT This article presents a circuit simulation-based design method for common-mode (CM) transformer-less hybrid EMI filters (HEFs) to obtain the required CM current attenuation. First, a simulation-based design method of the HEF, including the passive filtering components, is presented. The prototype HEF is implemented in a DC-fed three-phase motor drive system to validate the design method and evaluate the HEF's performance. The measured results validate the presented design method and show that the HEF can increase the CM current attenuation of a passive EMI filter (PEF) up to 8.2 dB in the frequency range from 100 kHz to 1.4 MHz. Furthermore, the measured result clarifies that implementing a voltage-sensing parallel-compensating active feedback circuit can reduce the volume of the CMI used in a PEF designed to achieve the same attenuation of the HEF by about 75 %.

INDEX TERMS Common-mode current, common-mode inductor, EMI, hybrid EMI filter.

I. INTRODUCTION

With the ever-increasing demand for high-power density, wide-bandgap semiconductor power devices with high-speed switching capability play an essential role in power electronics systems [1]. As switching speeds and frequencies increase, the electromagnetic noise generated by switching sequences of power devices increases [2], [3], [4], [5], [6]. As a result, electromagnetic interference (EMI), which may cause malfunctions of peripheral electronic devices, becomes more serious. Therefore, there is concern that EMI filters will become more extensive to satisfy the noise standard established by the International Electrotechnical Commission (IEC) in power electronics systems.

In order to reduce the size of passive EMI filters (PEFs), which consist only of passive components, hybrid EMI filters (HEFs), which combine the PEF and an active feedback (AFB) circuit based on bipolar transistors or operational amplifiers, have been proposed [7], [8], [9], [10], [11], [12], [13], [14]. As shown in Fig. 1, AFB circuits can be classified into four major categories based on noise sensing and compensating methods [6]. In Fig. 1, v_n is a noise voltage source, v_c is a compensating voltage source. Z_{load} and Z_{line} are load- and line-side impedances. Except for the voltage-sensing parallel-compensating (VSPC) type AFB circuits, every AFB circuit requires common-mode transformers (CMTs) for sensing and/or compensating high-frequency common-mode (CM) noise [10], [11]. To achieve good filtering performance, it is necessary to realize the CMT with a wide bandwidth. However, simply adding an extra winding in a conventional CM inductor (CMI) does not always guarantee high magnetic coupling over wideband frequencies due to safety regulations and the frequency dependence of the complex permeability of magnetic materials [15], [16], [17], [18], [19]. In addition, tightly windings for high magnetic coupling may increase winding stray capacitance and degrade the HF properties of the CMT [20], [21], [22], [23]. The large volume of a CMT compared to capacitors is also a drawback of using CMTs. On the other hand, the VSPC AFB-based HEF may realize wider operational bandwidth and smaller size than the other three types by using capacitors for noise sensing and compensating. For these reasons, the VSPC-type AFB circuit

The associate editor coordinating the review of this manuscript and approving it for publication was Jahangir Hossain.

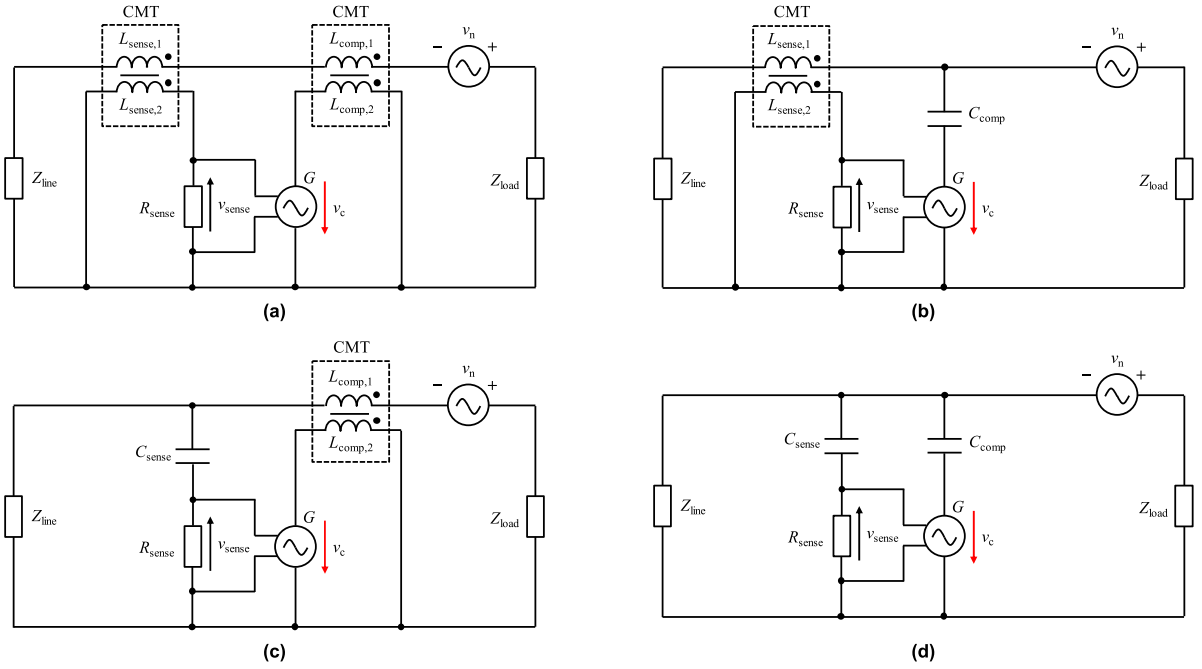

FIGURE 1. Basic structures of AFB circuits. (a) Current-sensing series-compensating type. (b) Current-sensing parallel-compensating type. (c) Voltage-sensing series-compensating type. (d) Voltage-sensing parallel-compensating type.

based on capacitive sensing and compensating is selected in this article.

The VSPC-type AFB-based HEF has been proposed for three-phase system in [10]. This HEF uses many bipolar transistors to construct the AFB circuit, which makes the HEF complex. Reference [11] has proposed the CMT-less HEF to reduce motor-side CM voltage in the higher frequency range beyond 30 MHz. In [12], the CMT-less HEF has been proposed to suppress the motor-side CM current. In this HEF, the compensation current is generated by applying the sensed CM voltage to the CM impedance matching circuit. Through the compensation current which has the same magnitude with opposite phase to the original CM current in the system, the line-side CM noise can be suppressed. The technical difficulty with this approach is that CM impedance matching over a wideband frequency is not always available. The operational amplifier-based CMT-less HEF proposed in [13], but the CM noise sensing is realized by a sensing resistor. Thus, it is difficult to use this HEF in high-power systems. Moreover, to the authors' knowledge, no literature presents a comprehensive design procedure for HEFs, including the design of passive components. In [14], the simulation-based design of voltage-sensing series-compensating type HEFs has been presented. However, minimum design of CMIs has not been addressed.

This article presents a simulation-based design method for CMT-less VSPC AFB-based HEFs to obtain the required CM current attenuation. The proposed design introduces a frequency-dependent inductor model to simulate the wideband frequency characteristic of nanocrystalline core-based CMIs. In addition, a CM equivalent circuit model of an experimental system is constructed based on the CM impedance measurement results. Combining these models allows the CM attenuation characteristic when the designed EMI filter is connected to the experimental system to be simulated over wideband frequencies. Moreover, an identification procedure of a minimum volume of CMI with single-layer windings to achieve desired CM current attenuation characteristic is presented. According to the presented design method, a prototype HEF is implemented in a DC-fed three-phase motor drive system, and the CM current attenuation characteristics are evaluated to demonstrate the validity of the design.

The rest of this article is organized as follows. In section II, a CM equivalent circuit of the experimental system is constructed on LTspice. Section III presents a simulation-based design procedure of the HEF. Note that a frequency-dependent CMI model is used in the simulation. Section IV evaluates the CM current attenuation characteristic of the prototyped HEF in the DC-fed three-phase motor drive system. The measurement results show that the HEF can increase the CM current attenuation of the PEF by up to 8.2 dB in the frequency range from 100 kHz to 1.4 MHz. Furthermore, it is confirmed that the application of the AFB circuit reduces the volume of CMI used in a PEF designed to achieve the same attenuation of the HEF by about 75%. Finally, Section V summarizes this article.

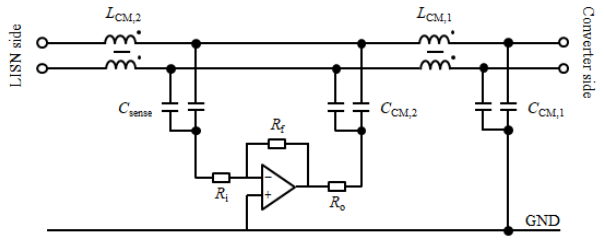

FIGURE 2. Configuration of the CMT-less HEF.

II. CONFIGURATION AND BASIC PRINCIPLE OF CMT-LESS HEF

Fig. 2 shows the configuration of the proposed CMT-less HEF. The HEF is connected to the input side of a DC-fed three-phase motor drive system. CMIs $L_{CM,1}$ and $L_{CM,2}$, and Y-capacitors $C_{CM,1}$ and $C_{CM,2}$, form a two-stage PEF. The VSPC-type AFB circuit consists of a sensing capacitor C_{sense}, a current feedback operational amplifier THS3001 (Texas Instruments), an input resistor R_i, a feedback resistor R_f, and an output resistor R_o.

Generally, first noise peak appearing beyond 150 kHz (most conducted EMI standard is regulated in the frequency range from 150 kHz to 30 MHz) gives required attenuation of EMI filters and determines the filter volume [24], [25]. Thus, suppression of low-frequency noise by using of the AFB circuit helps to decrease the volume of passive filtering components to satisfy the EMI standard. Following the above concept, the AFB circuit prefer to handle low-frequency components up to about 1 MHz. Moreover, the AFB circuit can easily handle the low-frequency noise without saturation of an amplifier output by decreasing high-frequency noise component properly due to the passive filter connected before the AFB circuit. Therefore, two-stage filter configuration is selected in this article.

In the CMT-less HEF with the configuration shown in Fig. 2, the first-stage Y-capacitor $C_{CM,1}$ returns CM current with a high-frequency of several MHz and a high amplitude of several amperes to the power converter. On the other hand, the Y-capacitor in the second stage of the PEF $C_{CM,2}$ only returns a low-frequency CM current of tens to hundreds of kHz and a small amplitude of about several tens of mA. Therefore, a high-speed operational amplifier of which the rated output current is several tens of mA can be implemented in the AFB circuit [26]. Since surface-mount components can be used for every component that forms the AFB circuit, they have little impact on the overall filter size.

Fig. 3(a) shows a simplified analytical model of the VSPC-type AFB circuit. The AFB circuit senses the CM voltage v_{in} through the high-pass filter composed of C_{sense} and R_i. The sensed CM voltage is multiplied by amplifier gain G, and the AFB circuit outputs the compensation voltage v_c. According to [11], an impedance of the Y-capacitor $C_{CM,2}$ ($Z_{CM,2}$) with the AFB is derived as

$$Z_{CM,2} = \frac{R_i + 1/sC_{sense}}{(1+G)\cdot R_i + 1/sC_{sense}} \cdot \frac{1}{sC_{CM,2}} \quad (1)$$

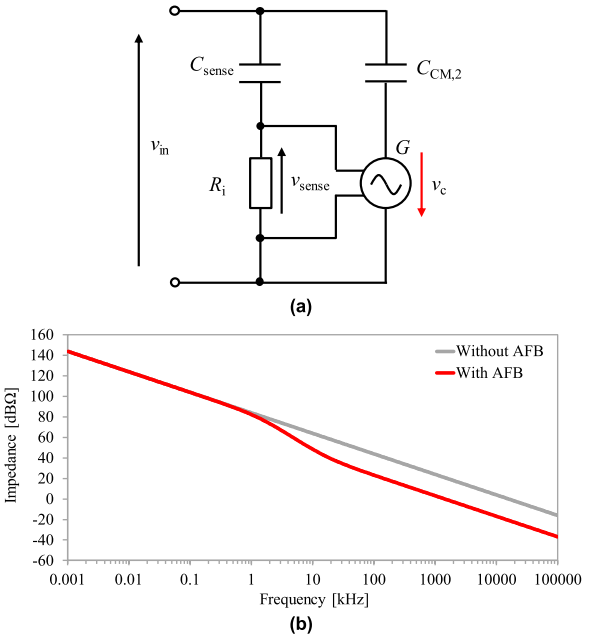

FIGURE 3. Basic principle of the AFB. (a) Simplified analytical model of the VSPC-type AFB circuit. (b) Calculated impedance of $C_{CM,2}$ when $C_{sense} = C_{CM,2} = 2 \times 4.7$ nF, $R_i = 1$ kΩ, and $G = 10$.

where, $s = j\omega$. The impedance of the input resistor is much smaller than that of the sensing capacitor in the high-frequency range. Thus, $Z_{CM,2}$ can be represented as

$$Z_{CM,2} \approx \frac{1}{1+G} \cdot \frac{1}{sC_{CM,2}} \quad (2)$$

Equation (2) shows that the capacitance of $C_{CM,2}$ is multiplied by amplifier gain G.

Fig. 3(b) shows the calculated impedances of $C_{CM,2}$ with or without the AFB. The calculated results indicates that the AFB circuit increases the capacitance of Y-capacitor in the high-frequency range. As a result, the cutoff frequency of the PEF can be shifted to a lower frequency range, and the attenuation in the high-frequency range can be increased without changing any passive components of the PEF [11].

III. DESIGN OF THE CMT-LESS HEF

A. COMMON-MODE EQUIVALENT CIRCUIT MODEL OF THE EXPERIMENTAL SYSTEM

A single-phase CM equivalent circuit model of a motor drive system under investigation is constructed on LTspice for evaluating the CM attenuation of the HEF. Fig. 4 shows the configuration of the experimental setup. A DC source is connected to a silicon-carbide (SiC) MOSFET-based three-phase pulse-width-modulation (PWM) inverter via a pair of line impedance stabilization networks (LISNs). The three-phase output terminals of the PWM inverter are connected to an induction motor of 0.75 kW via a 1 m unshielded three-core cable. The LISNs, inverter, and motor are placed on a ground plane. $C_{H,1}$ is the stray capacitance between the drain of high-side MOSFETs and the inverter heat sink, and

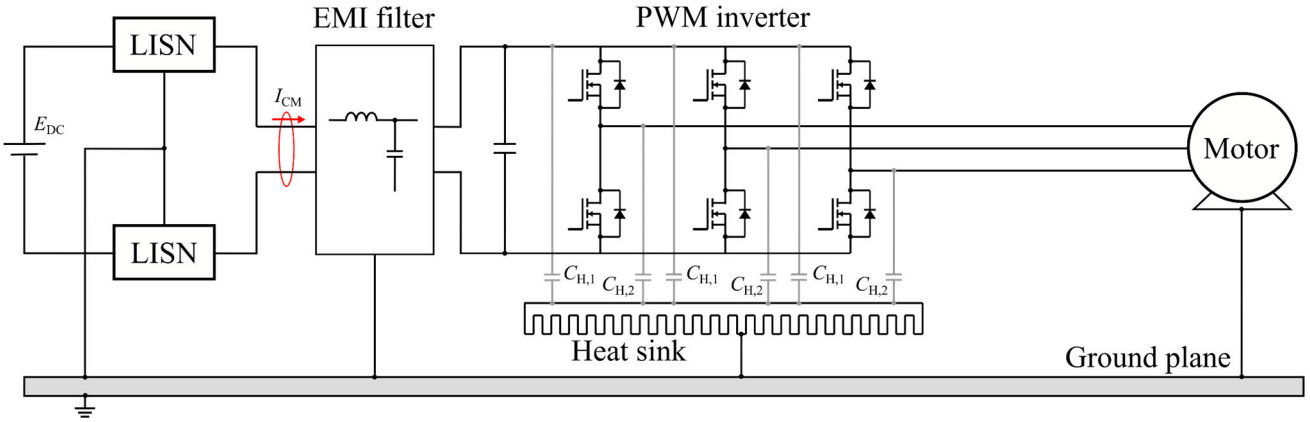

FIGURE 4. Configuration of the experimental system.

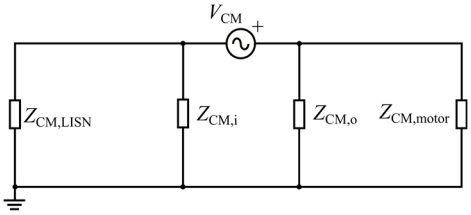

FIGURE 5. CM equivalent circuit model of the experimental system.

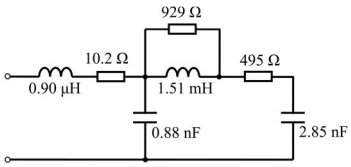

FIGURE 6. Identified CM equivalent circuit model of the motor.

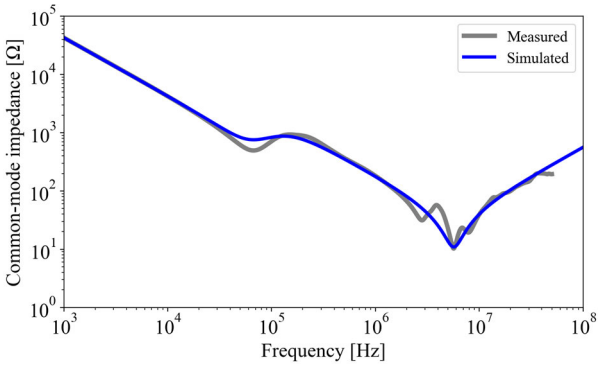

FIGURE 7. Measured and simulated motor CM impedances.

$C_{H,2}$ is the stray capacitance between the drain of low-side MOSFETs and the heat sink [27]. The inverter heat sink and the motor frame are connected to the ground plane via 0.1 m ground wires.

Fig. 5 shows the single-phase CM equivalent circuit of the experimental setup. $Z_{CM,LISN}$ is the LISN CM impedance and $Z_{CM,motor}$ is the motor CM impedance. $Z_{CM,i}$ is the sum of $C_{H,1}$ and $Z_{CM,o}$ is the sum of $C_{H,2}$. Here, v_u, v_v, and v_w in Fig. 4 are phase voltages with respect to the negative side of the DC link. The sum of voltages v_u, v_v, and v_w is not zero in three-phase PWM inverters [28]. Thus, the CM voltage source v_{CM}, which is the average of all phase voltages, is represented as

$$v_{CM} = \frac{v_u + v_v + v_w}{3} \tag{3}$$

An equivalent circuit of $Z_{CM,LISN}$ is derived from the datasheet. The other equivalent circuits of $Z_{CM,i}$, $Z_{CM,o}$, and $Z_{CM,motor}$ are constructed based on CM impedance measurements. Every impedance measurement is performed by using a network analyzer (Bode 100, Omicron Lab) and an impedance measurement fixture (B-WIC) in the frequency range from 1 kHz to 50 MHz. First, to identify $Z_{CM,i}$ and $Z_{CM,o}$, the LISN and motor are disconnected from the inverter, and an impedance between shorted output terminals of the inverter and the heat sink ground wire. Measured result indicates capacitive impedance of 300 pF up to 20 MHz. For simplicity, $Z_{CM,i}$ and $Z_{CM,o}$ are modeled as capacitors with values of 150 pF.

Next, to identify $Z_{CM,motor}$, the three-core output cable is disconnected at the output terminal of the inverter, and the impedance between a terminal where three phases of the cable are shorted and the motor ground wire. Based on the measured result, $Z_{CM,motor}$ is modeled by an equivalent circuit model shown in Fig. 6. A comparison between the measured $Z_{CM,motor}$ and the calculated result from the model is shown in Fig. 7. It can be confirmed from Fig. 7 that the calculated impedance matches the measured result over a wideband frequency.

B. DESIGN OF THE PASSIVE COMPONENTS IN THE SECOND STAGE OF THE PEF

This subsection describes the design procedure of $C_{CM,2}$ and $L_{CM,2}$ in the second stage of the PEF. The attenuation characteristics of the EMI filter depend on an impedance connected to the filter. In this article, $C_{CM,2}$ and $L_{CM,2}$ are

designed where the PEF can attenuate the CM noise in the frequencies above 100 kHz for any DC input side impedance. Note that the value of Y-capacitors is limited to prevent excessive leakage current to the ground [24], the designed value of $C_{CM,2}$ is 4.7 nF per phase for safety reason.

The CMI $L_{CM,2}$ is fabricated with a nanocrystalline core (Vitroperm 500F, Vaccumschmelze). Nanocrystalline core-based inductors behave as resistive components from several tens of kHz due to the frequency dependence in the complex permeability [16], [29], [30]. This resistive behavior damps self-resonance and ensures stability of the AFB circuit [10]. AL values of cores in the datasheet published by the manufacturer are calculated based on the permeabilities at specific frequencies. Therefore, the wideband attenuation of the PEF over a wideband frequency can only be evaluated at the design stage by considering the frequency-dependent complex permeability.

An inductor simulation model based on the permeance−capacitance (P−C) analogy couples the electric and magnetic circuit parts of the inductor using a gyrator [31], [32], [33]. The gyrator is an impedance inverting component realized using a pair of current-dependent voltage sources in circuit simulators. The magnetic circuit part of the model includes the permeance of the magnetic core, and the number of turns is implemented into the model as the gyrator gain. The frequency-dependent core permeance is modeled by three-stage RC ladder circuit in the magnetic circuit of the model as shown in Fig. 8. Modeling components R_1, R_2, R_3, C_1, C_2, and C_3 are identified from curve fitting result for measured and calculated complex permeability of the nanocrystalline core.

The P−C analogy-based model of the nanocrystalline core and $C_{CM,2}$ are implemented in an equivalent circuit model of the experimental system built on LTspice. $C_{CM,2}$ is a surface-mount component with low parasitic impedance and is assumed to be an ideal capacitor in the filter design. The attenuation characteristics of the filter are calculated as the ratio of the input side CM current with and without the filter connected. A parametric analysis is performed on the gyrator gain to identify the minimum number of turns to achieve the required attenuation characteristics.

For the design of the minimum volume CMI, it is necessary to select a minimum core with a window area that is large enough to allow the required number of turns. Note that a single-layer winding is selected to minimize winding stray capacitances of the CMI [34]. First, the conductor cross-sectional area of the wire A_w can be expressed by the following equation.

$$A_w = \pi \left(\frac{d_w}{2}\right)^2 \tag{4}$$

where, d_w is the conductor diameter of the wire, and is represented as

$$d_w = 2\sqrt{\frac{A_w}{\pi}} \tag{5}$$

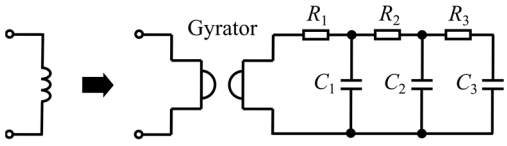

FIGURE 8. Permeance−capacitance analogy-based inductor model.

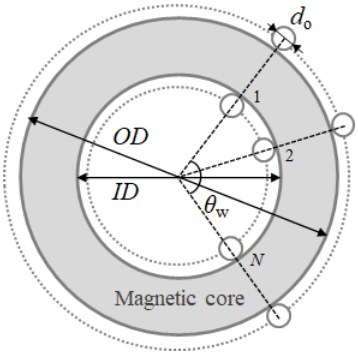

FIGURE 9. Cross-sectional view of a toroidal inductor.

The current density of the wire J_w is

$$J_w = \frac{I_{rms}}{A_w} \tag{6}$$

where, I_{rms} is the rms value of the current flows through the phase winding of the CMI.

The conductor cross-sectional area A_w is required to satisfy the following condition.

$$A_w \geq \frac{I_{rms}}{J_w} \tag{7}$$

Thus, the required conductor diameter of the wire is derived as

$$d_w \geq 2\sqrt{\frac{I_{rms}}{\pi J_w}} \tag{8}$$

The selected parameters are as follows: $I_{rms} = 5$ A, $J_w = 5$ A/mm^2. Pick $d_w = 1.20$ mm for the wire of $L_{CM,2}$.

As illustrated in Fig. 9, the wire diameter including an insulated coating d_o and the number of turns N needs to satisfy the following relationship.

$$N \cdot d_o \leq \left(\frac{ID}{2} - \frac{d_o}{2}\right)\theta_w \tag{9}$$

where, θ_w is the angle that one phase winding covers the toroidal core, and ID is the inner diameter of the toroidal core.

Thus, the required core size is obtained as

$$ID \geq \frac{2N \cdot d_o}{\theta_w} + d_o \tag{10}$$

The angle θ_w should be little less than $5\pi/6$ to ensure an insulating between the adjacent phase windings [34]. Under the above assumption, the core with minimum size which is enough to allow the required turns obtained from the parametric analysis on LTspice.

T60006-L2012-W902 nanocrystalline toroidal core is selected for the core of $L_{CM,2}$, and the turn number of phase winding is $N = 4$. Fig. 10 shows the simulated attenuation characteristic of the designed PEF consists of $L_{CM,2}$ and $C_{CM,2}$. It can be confirmed that the designed PEF has the CM attenuation in the frequencies above 100 kHz.

C. DESIGN OF THE PASSIVE COMPONENTS IN THE FIRST STAGE OF THE PEF

The design of $C_{CM,1}$ and $L_{CM,1}$ in the first stage of the PEF is performed in this subsection. $C_{CM,1}$ and $L_{CM,1}$ are designed where the two-stage PEF has the CM attenuation of 30 dB at 300 kHz. For safety reason, the value of $C_{CM,1}$ is also limited. Here, $C_{CM,1} = C_{CM,2} = 4.7$ nF per phase is selected.

$C_{CM,1}$, $C_{CM,2}$, and the model of $L_{CM,2}$ constructed in the previous subsection are implemented to the CM equivalent circuit model of the motor drive system. Moreover, the P−C analogy-based model of $L_{CM,1}$ is added to the simulation model, and the CM attenuation characteristic of the two-stage PEF is simulated. The parametric analysis for the gyrator gain in the model of $L_{CM,1}$ is performed, and the required turn number is identified. According to the constraint condition described in the previous subsection, the minimum core which is large enough to allow the required turn numbers of windings is find out.

As a result, T60006-L2016-W403 nanocrystalline core is selected for the core of $L_{CM,1}$, and the turn number is $N = 7$. Fig. 11 shows the simulated CM attenuation characteristic of the designed two-stage PEF. It can be confirmed that the designed PEF has the attenuation of −31.1 dB at 300 kHz and satisfies the design requirement.

D. DESIGN OF THE ACTIVE FEEDBACK CIRCUIT

At last, the simplified design of the AFB circuit is performed in this subsection. As described the above, in the VSPC AFB circuit, the sensing capacitor C_{sense} and the input resistor of the operational amplifier R_i form the high-pass filter.

The impact of the AFB on the Y-capacitor impedance appears in the higher frequencies than the high-pass cut-off frequency $f_{hi,cut}$. Thus, the values of C_{sense} and R_{in} are selected so that $f_{hi,cut}$ is less than 100 kHz.

$f_{hi,cut}$ is calculated as

$$f_{hi,cut} = \frac{1}{2\pi R_i \cdot 2C_{sense}} \tag{11}$$

For simplicity, $C_{sense} = C_{CM,1} = C_{CM,2} = 4.7$ nF per phase is selected. The value of R_i should be determined by considering the value of the feedback resistance R_f in addition to the high-pass filter cutoff frequency. The use of the small feedback resister may decrease the stability of the AFB circuit in the high-frequency range in current-feedback type operational amplifiers. Thus, the value of R_f should be set to several kΩ. Here, the feedback gain $G = 2$, $R_i = 1$ kΩ, and $R_f = 2$ kΩ are selected. At this condition, the high-pass cutoff frequency $f_{hi,cut}$ is 16.9 kHz. Furthermore, the output resistance R_o is recommended to use for increasing the stability of the AFB circuit with driving a capacitive load. Based on the datasheet of THS3001 (Texas Instruments) [35], $R_o = 20$ Ω is picked.

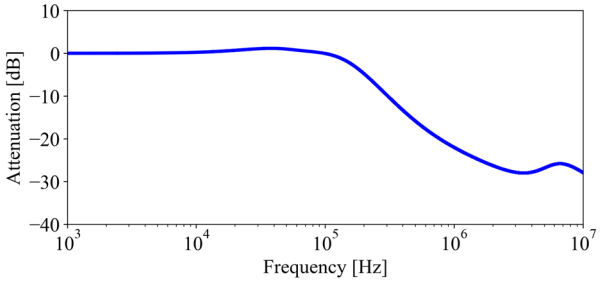

FIGURE 10. Simulated attenuation characteristic of the designed PEF consists of $L_{CM,2}$ and $C_{CM,2}$.

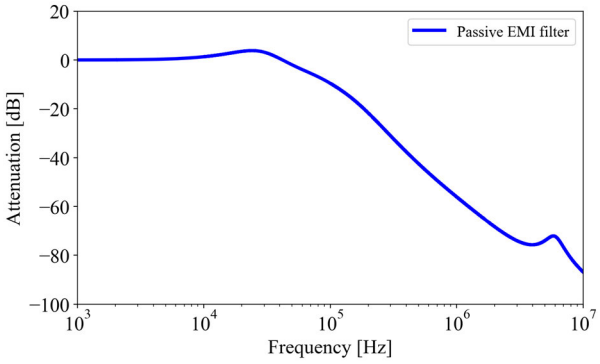

FIGURE 11. Simulated attenuation characteristic of the designed two-stage PEF consists of $L_{CM,2}$, $C_{CM,2}$, $L_{CM,1}$, and $C_{CM,1}$.

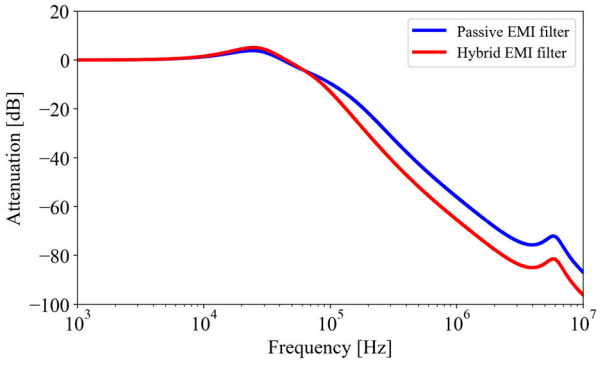

FIGURE 12. Simulated attenuation characteristic of the designed PEF and HEF.

A CM attenuation characteristic of the designed HEF is simulated on LTspice. SPICE model of THS3001 provided by the manufacturer is used for the simulation model of the AFB circuit. A comparison of the simulated CM attenuation characteristics of the PEF and HEF is shown in Fig. 12.

Fig. 12 indicates that the attenuation of HEF is about 10 dB greater than that of PEF in the frequency range from 100 kHz to 10 MHz. Moreover, the attenuation of the HEF at 300 kHz is about −40.5 dB, which is 9.4 dB greater than that of the PEF.

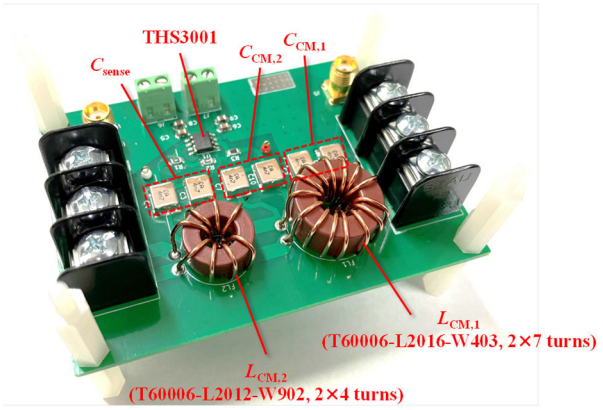

FIGURE 13. Prototype of the CMT-less HEF.

The prototype of the -less HEF based on the design performed in this section is shown in Fig. 13. Since the AFB circuit consists of surface-mount components, adding the AFB circuit to a printed circuit board has little impact on the overall filter size. Note that a floating DC power supply (±15 V) is used for a power source of the operational amplifier in the prototyped HEF for simplicity of experiments. However, a low-cost small size constant voltage circuit introduced in [9] can be used to supply the HEF in the practical use.

IV. EXPERIMENTAL VALIDATION

A. INSERTION LOSS

First, insertion losses of the fabricated PEF and HEF were measured by using the network analyzer in the frequency range from 10 kHz to 10 MHz. The measured insertion loss curves are shown in Fig. 14. The measured results show that the attenuation of the HEF is higher than that of the PEF from around 70 kHz. These results validate the design of the AFB circuit presented in subsection III-D. In frequencies higher than 3 MHz, attenuation characteristics deteriorate due to the self-resonances of filtering passive components.

Furthermore, the frequency-domain simulations performed on LTspice according to the configuration shown in Fig. 15. The voltages v_{o1} when no filter is connected and the voltage v_{o2} when the filter is connected were simulated. From v_{o1} and v_{o2}, the insertion loss IL is derived as

$$IL = 20\log_{10}\frac{v_{o2}}{v_{o1}} \tag{12}$$

Figs. 16(a) and 16(b) show comparison results of measured and simulated insertion losses. The simulated results when the CMIs were modeled as ideal inductors are also shown as "Datasheet-based model" in Figs. 16(a) and 16(b). In datasheet-based models, the CM inductances of the CMIs were calculated based on the AL values at 10 kHz obtained from the datasheet. Figs. 16(a) and 16(b) clarify that the proposed simulation model, including the frequency-dependent CMI models, can simulate the attenuation characteristics of filters over a wideband frequency. On the contrary, the simulated results from datasheet-based models do not match the

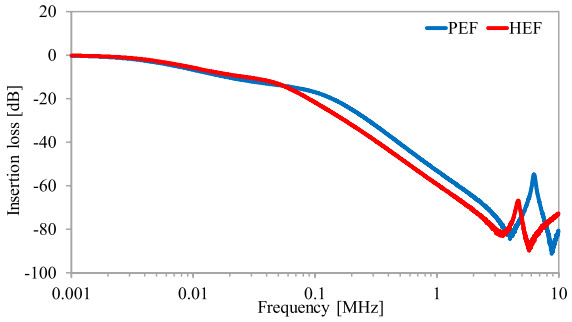

FIGURE 14. Measured insertion losses of the PEF and HEF.

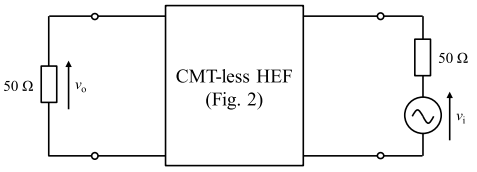

FIGURE 15. Configuration for simulating insertion losses.

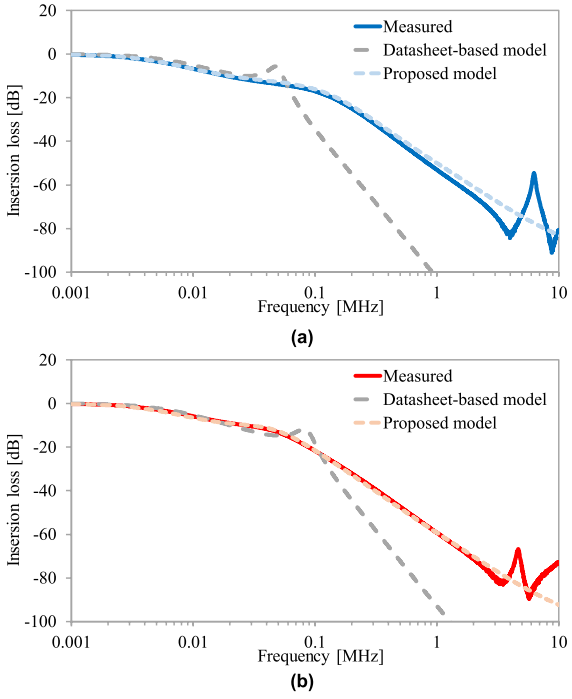

FIGURE 16. Comparison of measured and simulated insertion losses. (a) PEF. (b) HEF.

measured result in the high-frequency range. It should be noted that the proposed models can not simulate the attenuation characteristics of each filter in higher frequencies than around 3 MHz because the proposed models do not include stray impedances of passive components.

B. CM CURRENT ATTENUATION CHARACTERISTIC

Next, to evaluate the validity of the design and the CM current attenuation characteristics of the CMT-less HEF, CM current measurements were performed on the experimental system.

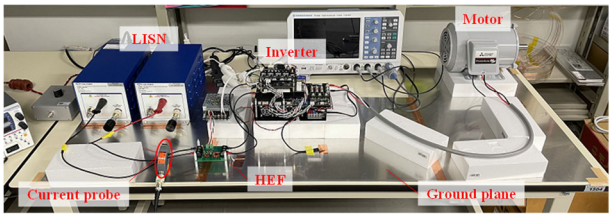

FIGURE 17. Experimental system.

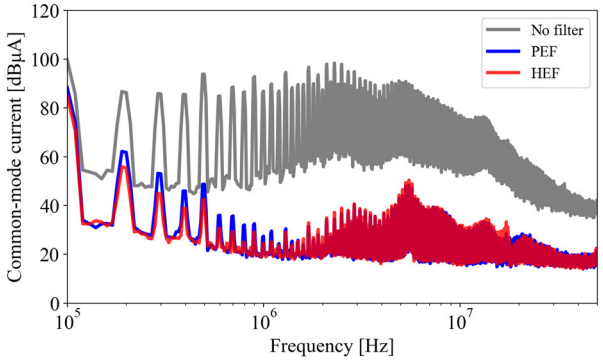

FIGURE 18. Comparison of measured CM currents.

Fig. 17 shows the experimental system constructed at the laboratory. The three-phase PWM inverter, the motor with no load, and input/output cables were placed on the ground plane through 5 cm-thick Styrofoam blocks. For all measurements performed in this article, the output voltage of the DC power supply was 200 V, the switching frequency of the inverter was 100 kHz, the output frequency was 50 Hz, and the modulation index was 0.5.

CM currents were measured by a spectrum analyzer (FPL1003, ROHDE&SCHWARZ) using a current monitor probe (F-33-2, FCC) with the input cable clamped as a whole. Since the spectrum analyzer displays voltage values, the CM currents were obtained by making corrections based on the transformer impedance of the probe. Measurements were performed when no filter was connected, the PEF was connected, and the HEF was connected.

The measured CM currents are shown in Fig. 18. It can be confirmed that the HEF increases the attenuation of the PEF in the frequency range from 100 kHz to 1.4 MHz. The measured attenuations of the PEF and HEF at 300 kHz are −32.7 dB and −40.9 dB, which results are almost equal to the designed values. These measurement results fully satisfy the design concept of the HEF described in this article. The maximum attenuation improvement by applying the AFB circuit to the PEF is around 8.2 dB at 300 kHz. The higher attenuation can be achieved by increasing the amplifier gain. One of the purposes of this article is to demonstrate the proposed simulation-based HEF design method. Therefore, the amplifier gain G is set to relatively low ($G = 2$), so the improvement of the CM attenuation by adding the AEF circuit is limited. In the frequency range above 1.4 MHz, unlike the simulation results presented in the

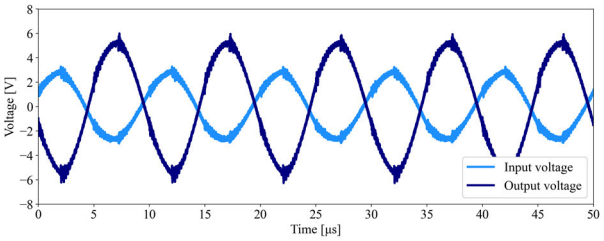

FIGURE 19. Measured input and output waveforms of the AFB circuit.

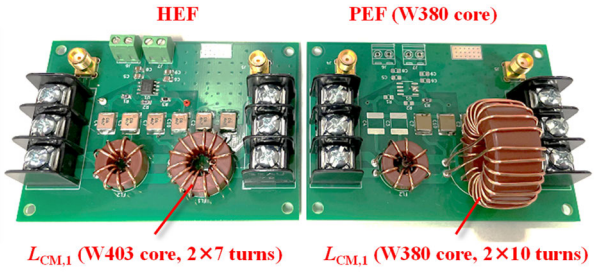

FIGURE 20. Size comparison of CMIs between the PEF and HEF.

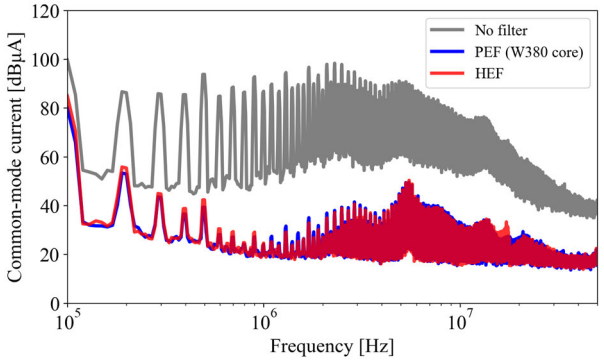

FIGURE 21. Comparison of measured CM currents when the W380 core with ten turns was used for $L_{CM,1}$ of the PEF.

previous section, the CM current attenuation characteristics of the PEF and HEF are almost equal. The difference between the simulated and measured results is possibly related to stray impedances not considered in the simulation, as shown in Figs. 16(a) and 16(b).

Fig. 19 shows the measured input/output voltage waveforms of the AFB circuit. It can be observed that the AFB circuit outputs an inverted amplified waveform without causing output saturation of the operational amplifier.

According to the design described in Section III, the PEF with the same attenuation of the HEF at 300 kHz can be realized by $L_{CM,1}$ selecting T60006-L2025-W380 nanocrystalline core (W380 core) with ten turns per phase winding. Fig. 20 shows a picture of the HEF and redesigned PEF.

Fig.21 shows the measured CM currents when no filter is connected, the redesigned PEF is connected, and the HEF is connected. The attenuation of the PEF with the W380 core at 300 kHz is −42.3 dB, almost equal to that of the HEF with

the W403 core. The volume of the W403 core implemented in the HEF is 574 mm^3, and that of the W380 core used in the PEF is 2304 mm^3. Therefore, the core volume of CMI can be reduced by about 75 % by applying the AFB.

V. CONCLUSION

In this article, a comprehensive design method of the CMT-less VSPC AFB-based HEF has been given. By incorporating the HEF model into the CM equivalent circuit model of the DC-fed three-phase motor drive system, the filter attenuation characteristic can be simulated. Based on the simulation, the comprehensive design of the HEF is introduced, including a design procedure for the minimum CMI to achieve the required attenuation. The CM current measurement results demonstrate the proposed design of the HEF. The design method proposed in this article can be applied not only to DC-fed three-phase motor drive systems but also to all other power conversion systems. Specifically, the contributions are:

1) Proposed the two-stage CMT-less HEF, which has a simple structure compared to the conventional design. Experimental results verified that the proposed HEF can reduce the volume of CMI used in the PEF designed to achieve the same attenuation of the HEF by about 75 %.

2) Developed the frequency-domain simulation model of the HEF, including the motor drive system and frequency-dependent CMI models.

3) Developed the simulation-based design method of the HEF with minimum volume CMI to achieve the required attenuation.

The design and stability analysis of HEFs considering stray impedances is the next step of this study.

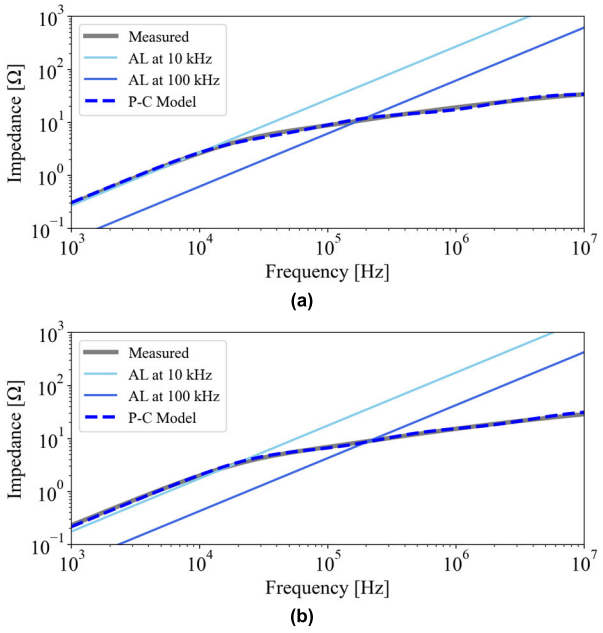

FIGURE 22. Measured and simulated impedance of inductors with 1 turn. (a) W403 core. (b) W902 core.

TABLE 1. Model parameters of permeance-capacitance analogy-based inductor models.

Part number	T60006-L2016-W403	T60006-L2012-W902
R_1	2.82×10^{-2} [Ω]	2.84×10^{-2} [Ω]
R_2	5.00×10^{-2} [Ω]	4.69×10^{-2} [Ω]
R_3	2.34×10^{-1} [Ω]	1.42×10^{-1} [Ω]
C_1	2.91×10^{-6} [F]	1.57×10^{-6} [F]
C_2	1.78×10^{-5} [F]	7.71×10^{-6} [F]
C_3	2.80×10^{-5} [F]	2.52×10^{-5} [F]

APPENDIX

The data sheets of the nanocrystalline cores used in this article provide AL values at 10 kHz and 100 kHz. Fig. 22 compares the calculated one-turn inductor impedance of the W403 and W902 cores based on AL values, the simulation results based on the P−C analogy-based model, and the measurement results, respectively. Model parameters of the simulation models are listed in Table 1. It can be confirmed that the calculated result using the AL value at 10 kHz shows almost no difference from the measured impedance up to about 20 kHz. However, in the frequency range above 20 kHz, the difference between the calculated and measured results increases. Moreover, the calculated result using the AL value at 100 kHz shows a significant difference between the calculated and measured results over the entire frequency range. On the other hand, Fig. 22 validates that the P−C analogy-based inductor model can simulate the impedance of nanocrystalline core-based inductors over the wideband frequency range.

REFERENCES

[1] J. Biela, M. Schweizer, S. Waffler, and J. W. Kolar, "SiC versus Si—Evaluation of potentials for performance improvement of inverter and DC–DC converter systems by SiC power semiconductors," *IEEE Trans. Ind. Electron.*, vol. 58, no. 7, pp. 2872–2882, Jul. 2011.

[2] D. Han, C. T. Morris, W. Lee, and B. Sarlioglu, "Comparison between output CM chokes for SiC drive operating at 20- and 200-kHz switching frequencies," *IEEE Trans. Ind. Appl.*, vol. 53, no. 3, pp. 2178–2188, May/Jun. 2017.

[3] D. Han, S. Li, Y. Wu, W. Choi, and B. Sarlioglu, "Comparative analysis on conducted CM EMI emission of motor drives: WBG versus Si devices," *IEEE Trans. Ind. Electron.*, vol. 64, no. 10, pp. 8353–8363, Oct. 2017.

[4] G. Engelmann, A. Sewergin, M. Neubert, and R. W. De Doncker, "Design challenges of SiC devices for low- and medium-voltage DC–DC converters," *IEEJ J. Ind. Appl.*, vol. 8, no. 3, pp. 505–511, May 2019.

[5] B. Zhang and S. Wang, "A survey of EMI research in power electronics systems with wide-bandgap semiconductor devices," *IEEE J. Emerg. Sel. Topics Power Electron.*, vol. 8, no. 1, pp. 626–643, Mar. 2020.

[6] S. Takahashi, K. Wada, H. Ayano, S. Ogasawara, and T. Shimizu, "Review of modeling and suppression techniques for electromagnetic interference in power conversion systems," *IEEJ J. Ind. Appl.*, vol. 11, no. 1, pp. 7–19, 2022.

[7] W. Chen, X. Yang, and Z. Wang, "An active EMI filtering technique for improving passive filter low-frequency performance," *IEEE Trans. Electromagn. Compat.*, vol. 48, no. 1, pp. 172–177, Feb. 2006.

[8] M. Li, M. Shen, L. Xing, and W. Said, "Current feedback based hybrid common-mode EMI filter for grid-tied inverter application," in *Proc. IEEE Energy Convers. Cong. Expo.*, Sep. 2012, pp. 1394–1398.

[9] M. Ali, E. Labouré, and F. Costa, "Integrated active filter for differential-mode noise suppression," *IEEE Trans. Power Electron.*, vol. 29, no. 3, pp. 1053–1057, Mar. 2014.

[10] M. L. Heldwein, H. Ertl, J. Biela, and J. W. Kolar, "Implementation of a transformerless common-mode active filter for offline converter systems," *IEEE Trans. Ind. Electron.*, vol. 57, no. 5, pp. 1772–1786, May 2010.
[11] S. Takahashi, S. Ogasawara, M. Takemoto, K. Orikawa, and M. Tamate, "Common-mode voltage attenuation of an active common-mode filter in a motor drive system fed by a PWM inverter," *IEEE Trans. Ind. Appl.*, vol. 55, no. 3, pp. 2721–2730, May 2019.
[12] Y. Zhang, Q. Li, and D. Jiang, "A motor CM impedance based transformerless active EMI filter for DC-side common-mode EMI suppression in motor drive system," *IEEE Trans. Power Electron.*, vol. 35, no. 10, pp. 10238–10248, Oct. 2020.
[13] Z. Zhang and A. M. Bazzi, "A virtual impedance enhancement based transformer-less active EMI filter for conducted EMI suppression in power converters," *IEEE Trans. Power Electron.*, vol. 37, no. 10, pp. 11962–11973, Oct. 2022.
[14] D. Shin, S. Jeong, Y. Baek, C. Park, G. Park, and J. Kim, "A balanced feedforward current-sense current-compensation active EMI filter for common-mode noise reduction," *IEEE Trans. Electromagn. Compat.*, vol. 62, no. 2, pp. 386–397, Apr. 2020.
[15] C. R. Sullivan and A. Muetze, "Simulation model of common-mode chokes for high-power applications," *IEEE Trans. Ind. Appl.*, vol. 46, no. 2, pp. 884–891, Mar./Apr. 2010.
[16] M. L. Heldwein, L. Dalessandro, and J. W. Kolar, "The three-phase common-mode inductor: Modeling and design issues," *IEEE Trans. Ind. Electron.*, vol. 58, no. 8, pp. 3264–3274, Aug. 2011.
[17] C. Cuellar, N. Idir, and A. Benabou, "High-frequency behavioral ring core inductor model," *IEEE Trans. Power Electron.*, vol. 31, no. 5, pp. 3763–3772, May 2016.
[18] M. Kacki, M. S. Rylko, J. G. Hayes, and C. R. Sullivan, "Magnetic material selection for EMI filters," in *Proc. IEEE Energy Convers. Cong. Expo.*, Oct. 2017, pp. 2350–2356.
[19] S. Takahashi, "Experimental investigation of the dimensional effect on small-signal characteristics of common-mode inductors," *IEEE Access*, vol. 10, pp. 123068–123079, 2022.
[20] A. Massarini and M. K. Kazimierczuk, "Self-capacitance of inductors," *IEEE Trans. Power Electron.*, vol. 12, no. 4, pp. 671–676, Jul. 1997.
[21] M. Kovacic, Z. Hanic, S. Stipetic, S. Krishnamurthy, and D. Zarko, "Analytical wideband model of a common-mode choke," *IEEE Trans. Power Electron.*, vol. 27, no. 7, pp. 3173–3185, Jul. 2012.
[22] S. W. Pasko, M. K. Kazimierczuk, and B. Grzesik, "Self-capacitance of coupled toroidal inductors for EMI filters," *IEEE Trans. Electromagn. Compat.*, vol. 57, no. 2, pp. 216–223, Apr. 2015.
[23] S. Takahashi and S. Maekawa, "Wideband small-signal model of common-mode inductors based on stray capacitance estimation method," *IEEJ J. Ind. Appl.*, vol. 11, no. 3, pp. 514–521, 2022.
[24] F.-Y. Shih, D. Y. Chen, Y.-P. Wu, and Y.-T. Chen, "A procedure for designing EMI filters for AC line applications," *IEEE Trans. Power Electron.*, vol. 11, no. 1, pp. 170–181, Jan. 1996.
[25] K. Raggl, T. Nussbaumer, and J. W. Kolar, "Guideline for a simplified differential-mode EMI filter design," *IEEE Trans. Ind. Electron.*, vol. 57, no. 3, pp. 1031–1040, Mar. 2010.
[26] S. Wang, Y. Y. Maillet, F. Wang, D. Boroyevich, and R. Burgos, "Investigation of hybrid EMI filters for common-mode EMI suppression in a motor drive system," *IEEE Trans. Power Electron.*, vol. 25, no. 4, pp. 1034–1045, Apr. 2010.
[27] H. Akagi and T. Doumoto, "A passive EMI filter for preventing high-frequency leakage current from flowing through the grounded inverter heat sink of an adjustable-speed motor drive system," *IEEE Trans. Ind. Appl.*, vol. 41, no. 5, pp. 1215–1223, Sep./Oct. 2005.
[28] S. Ogasawara and H. Akagi, "Modeling and damping of high-frequency leakage currents in PWM inverter-fed AC motor drive systems," *IEEE Trans. Ind. Appl.*, vol. 32, no. 5, pp. 1105–1114, Sep./Oct. 1996.
[29] M. Hartmann, H. Ertl, and J. W. Kolar, "EMI filter design for a 1 MHz, 10 kW three-phase/level PWM rectifier," *IEEE Trans. Power Electron.*, vol. 26, no. 4, pp. 1192–1204, Apr. 2011.
[30] A. Roc'h and F. Leferink, "Nanocrystalline core material for high-performance common mode inductors," *IEEE Trans. Electromagn. Compat.*, vol. 54, no. 4, pp. 785–791, Aug. 2012.
[31] P. G. Blanken and J. J. L. M. Van Vlerken, "Modeling of electromagnetic systems," *IEEE Trans. Magn.*, vol. 27, no. 6, pp. 4509–4515, Nov. 1991.
[32] L. Dalessandro, W. G. H. Odendaal, and J. W. Kolar, "HF characterization and nonlinear modeling of a gapped toroidal magnetic structure," *IEEE Trans. Power Electron.*, vol. 21, no. 5, pp. 1167–1175, Sep. 2006.
[33] J. Allmeling, W. Hammer, and J. Schönberger, "Transient simulation of magnetic circuits using the permeance-capacitance analogy," in *Proc. IEEE 13th Workshop Control Modeling Power Electron. (COMPEL)*, Jun. 2012, pp. 1–6.
[34] D. Han, C. T. Morris, W. Lee, and B. Sarlioglu, "Three-phase common mode inductor design and size minimization," in *Proc. IEEE Transp. Electrific. Conf. Expo (ITEC)*, Jun. 2016, pp. 1–8.
[35] *420-MHz High-Speed Current-Feedback Amplifier THS3001*, Texas Instrum., Dallas, TX, USA, Sep. 2009.

SHOTARO TAKAHASHI (Member, IEEE) was born in Hokkaido, Japan. He received the B.S., M.S., and Ph.D. degrees in electrical engineering from the Graduate School of Information Science and Technology, Hokkaido University, Japan, in 2015, 2017, and 2020, respectively.

From April 2020 to March 2021, he was a Project Assistant Professor with Tokyo Metropolitan University, Hachioji, Tokyo, Japan. From April 2021 to March 2023, he was an Assistant Professor with Seikei University, Kichijoji, Tokyo. Since April 2023, he has been a Lecturer with Akita University, Akita, Japan. His research interests include the electromagnetic interference (EMI) of high-frequency switching power converters, passive/active hybrid EMI filters, and modeling of magnetic components. He is a member of the Institute of Electrical Engineers of Japan (IEEJ) and the Institute of Electronics, Information and Communication Engineers (IEICE). He was a recipient of the 20th International Conference on Electrical Machines and Systems (ICEMS2017) Best Paper Award in 2017 and the IEEJ Industry Applications Society Distinguished Transaction Paper Award in 2018.